Glass-forming ability and ZrO2 saturation limits in the magnesium aluminosilicate system

Alessio Zandonà, Marine Moustrous, Cécile Genevois, Emmanuel Véron, Aurélien Canizarès, Mathieu Allix

Glass-forming ability and ZrO_2 saturation limits in the magnesium aluminosilicate system

Alessio Zandonà[1,*], Marine Moustrous[1], Cécile Genevois[1], Emmanuel Véron[1], Aurélien Canizarès[1], Mathieu Allix[1]

[1]CNRS, CEMHTI UPR3079, Univ. Orléans, F-45071 Orléans, France

Abstract

Containerless melting was employed to evaluate the influence of increasing ZrO_2 additions on the glass-forming ability of peraluminous melts in the magnesium aluminosilicate system. The saturation limit of this oxide in glasses along the silica-cordierite join (SiO_2–$Mg_2Al_4Si_5O_{18}$) is inversely proportional to the SiO_2 content; however, a limited solubility of ZrO_2 in melt-quenched silica exists (~2 mol%). Peraluminous samples (particularly MgO-free samples) exhibited a substantially higher capability of incorporating ZrO_2 without undergoing devitrification during cooling. TEM investigations revealed phase separation in all amorphous samples off the MgO = Al_2O_3 line, with ZrO_2 preferentially segregating into a SiO_2-depleted phase. These results identify the key role of Al_2O_3 for the structural incorporation of ZrO_2 in silicate melts, opening up alternative pathways for the development of glasses and glass-ceramics respectively based on the homogeneous distribution of ZrO_2 or, in turn, on its exploitation to induce phase separation and crystal nucleation.

Keywords: glass solubility, ZrO_2 nucleation, phase separation, glass-forming ability, containerless melting

*** Corresponding author:** alessio.zandona@cnrs-orleans.fr, +33(0)628331057

1. Introduction

ZrO_2-containing silicate melts remarkably constitute the common precursor for a variety of different functional materials. It is the case of electrofused refractory ceramics, whose long-lived chemical and thermal stability essentially relies on the complex assemblage of monoclinic ZrO_2 (m-ZrO_2) and α-Al_2O_3 crystallized from a parent melt during slow cooling [1]. As a widespread secondary component of glasses, ZrO_2 is moreover known to critically enhance their chemical durability [2,3], with a sensible impact on the corrosion mechanism of glasses for nuclear waste immobilization [4,5]. In glass-ceramics, ZrO_2 is additionally widely employed as a nucleating agent: during thermal annealing of the starting glass, it typically induces the early precipitation of nanosized tetragonal ZrO_2 crystals (t-ZrO_2) [6–11], which act as heterogeneous nucleation centers for the subsequent controlled crystallization of the silicate matrix. Intensive research efforts have been more recently directed to the development of glass-ceramics with high crystalline ZrO_2 contents [12–16], to obtain rare-earth-free photoluminescence [17] or in the attempt of replicating the well-known transformation toughening typically observed in conventional ZrO_2 ceramics [18].

For all of the above-mentioned applications, a strict control over devitrification during cooling from the molten state must be achieved, which is particularly challenging at very high ZrO_2 content. Although geoscientists already developed reliable models to estimate the solubility of ZrO_2 in silicate melts as a function of temperature and composition [19–23], the studied compositions differed markedly from those of technologically relevant materials; more importantly, glass-forming ability was never directly evaluated. This study aims therefore at providing an enhanced systematic understanding of the quenchability of ZrO_2-containing aluminosilicate glasses, to support the future compositional design of functional materials based on this metal oxide. To minimize heterogeneous surface nucleation of the silicate matrix and specifically examine the tendency of ZrO_2 to precipitate homogeneously

in the melts during quenching, we synthesized our samples by aerodynamic levitation coupled to laser heating (ADL) [24,25]. This containerless technique was indeed previously shown to enable the obtainment of exotic glasses with poor glass-forming ability (e.g. titanates, niobates and wolframates [26,27]). The results of our study complement the existing picture of the quaternary system MgO-Al_2O_3-SiO_2-ZrO_2 and of its inherent tendency towards heterogeneity and phase separation, introducing alternative compositional approaches in the quest for superior glasses and glass-ceramics.

2. Materials and methods

Table 1. Nominal glass compositions analyzed on the peraluminous side of the MgO–Al_2O_3–SiO_2 system, associated to all ZrO_2 contents (e.g. 8 mol% ZrO_2 + 92 mol% S55r1 in sample S55r1Zr8) tested to investigate their glass-forming ability. Devitrified compositions are marked by an *.

Sample name	Nominal composition of the base glass			ZrO_2 content(s) (mol%)
	MgO (mol%)	Al_2O_3 (mol%)	SiO_2 (mol%)	
S100	0	0	100	0, 0.75, 1.5, 2*, 4*
S85r1	7.5	7.5	85	0, 2, 4*, 8*
S85r0	0	15	85	0, 4
S75r1	12.5	12.5	75	0, 2, 4, 8*
S75r0.4	7	18	75	8
S75r0	0	25	75	0, 4, 8
S55r1	22.5	22.5	55	0, 4, 6, 8, 10, 15*, 20*
S55r0.5	14	31	55	15*
S55r0.2	7	38	55	15
S55r0	0	45	55	0, 8, 15

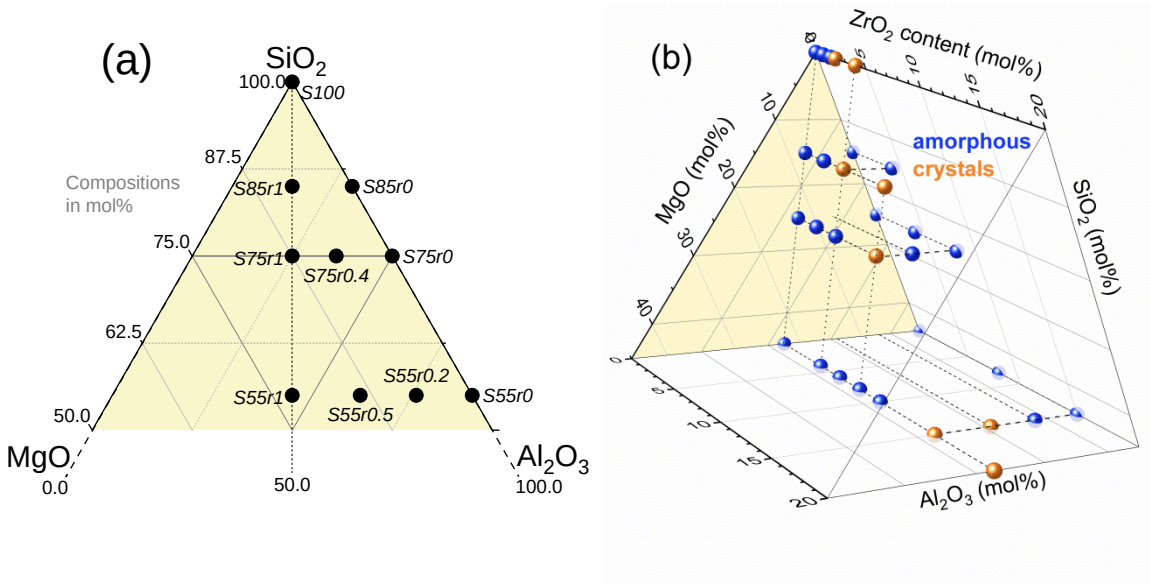

Figure 1. a) Upper section of the MgO-Al_2O_3-SiO_2 ternary diagram, reporting the base glass compositions analyzed within this work. b) Summary of all samples synthesized within this work (see also Table 1): partially devitrified materials (as concomitantly determined by XRD and Raman) are identified by orange spheres, while fully amorphous samples are shown in blue (mind that all amorphous samples off the line MgO = Al_2O_3 were investigated by TEM and found to exhibit phase separation; see Fig. 5 and related discussion).

2.1 Synthesis of the samples

Our study focused on the peraluminous side of the MAS system (see Tab. 1 and Fig. 1); attempts to extend the examination towards strongly subaluminous compositions invariably yielded opaque or devitrified samples. Base compositions S100, S85r1, S75r1 and S55r1 located on the silica-cordierite join, along which the MgO/Al_2O_3 molar ratio equals 1; other samples were then defined by substituting some (or all) their MgO with Al_2O_3. The chosen nomenclature reflected these compositional features, e.g. S55r0.2 for a sample with 55 mol% SiO_2 and MgO/Al_2O_3 = 0.2. An additional suffix manifested the addition of ZrO_2 (S55r0.2Zr15 for 15 mol% ZrO_2 added to 85 mol% S55r0.2 glass). All samples were synthesized using laboratory-grade raw materials: MgO (99.5%, Strem Chemicals), Al_2O_3

(99.999%, Strem Chemicals), SiO_2 (99.9%, Chempur) and ZrO_2 (99%, Koch-Light Laboratories). The final melt-quenching stage took place invariably by ADL in an Ar gas flow, using a top and a bottom CO_2 lasers (wavelength: 10.6 μm; maximum power: 250 W) to heat up the samples and two pyrometers to estimate their temperature; the average quenching rate was computed at ~250 K s^{-1} (see Figs. S1 and S2 in SI section). The synthesis protocol was however adjusted to each composition:

- in the case of the highly viscous S100 series, batches of 5 g (SiO_2+ZrO_2) were mixed for 3 h in an agate ball mill to achieve thorough homogenization. After this, the powders were pressed into pellets, from which small chunks (10-20 mg) were detached and melted by ADL at 1900-2100 °C for approximately 5 s; quenching was simply achieved by shutting off the lasers. After crushing and grinding the glassy (or devitrified) beads in a hand mortar, the procedure was repeated twice.
- given their lower melting temperature, S85r1, S75r1 and S55r1 were first produced as ZrO_2-free glasses by conventional furnace melting in Pt-Rh20 crucibles: after mechanical mixing for 3 h, batches of 4 g were heated at 1650 °C for 2 h, quenched, crushed and remelted to ensure homogeneity. After this, ZrO_2 was added to approximately 2 g of the obtained glasses and the double furnace melting at 1650 °C was repeated in the same way. Finally, all samples were melted once by ADL.
- the peraluminous samples, exhibiting high liquidus temperatures but comparatively low viscosity, were melted only once by ADL at 1900-2100 °C, after carefully mixing the starting powders in an agate hand mortar and pressing pellets of 1 g.

To compare the Raman features of ZrO_2 crystals formed during melt-quenching or secondary heat treatments, three glassy samples were additionally annealed in the furnace at selected temperatures: 15 min at 1000 °C for S75r1Zr4, 15 min at 900 °C for S55r1Zr8 and 1 h at 1000 °C for S55r0Zr15. We estimated these temperatures based on previous works

[28,29] and own DSC and high temperature XRD measurements (see Figs. S4 and S5 in the SI section). The three samples are labeled with an additional *–ht* suffix.

2.2 Raman Spectroscopy

The as-prepared glassy beads were measured on a Renishaw InVia Qontor spectrometer equipped with a green laser (514 nm) operating at 50 mW (the low-wavenumber cutoff of the edge filter is at ~100 cm^{-1}). After focusing 20-40 μm below the surface, the spectra were collected in the range 80-2000 cm^{-1} using a 1800 lines/mm holographic grating, with 15 s acquisition time and 6 repetitions. Laser power and acquisition time were occasionally lowered to avoid detector saturation in the case of highly crystalline materials. After applying a simple baseline, the spectra were normalized to their maximum intensity to facilitate comparison.

2.3 X-ray Diffraction (XRD)

XRD characterization was performed in Bragg-Brentano geometry using a D8 Advance Bruker laboratory diffractometer, equipped with a Cu X-ray tube and a LynxEye XE line detector. Single glassy beads were crushed and grinded in an agate hand mortar and the resulting powders were dispersed on low-background flat Si sample holders with the help of some ethanol drops. The measurements were run at 30 kV – 40 mA in the range 15-80 ° 2θ, with increments of 0.025 ° 2θ and 0.7 s for each step. In-situ high-temperature XRD measurements (Figure S3 of the SI section) were performed to identify suitable temperatures for the heat treatments described in Section 2.1, using Anton Paar's HTK1200N heating chamber. The powdered glass samples were deposited on a platinum disk to avoid any reaction with the underlying alumina crucible and data were collected every 50 °C between 600 °C and 1200 °C with Vantec-1 line detector.

2.4 Transmission electron microscopy (TEM)

Single beads were crushed and grinded in an agate hand mortar and the resulting powder was then dispersed in ethanol. A small drop of the suspension was loaded on a TEM copper grid layered by an amorphous holey carbon film and dried. Imaging of the samples and elemental analyses were performed with a Philips CM20 TEM operated at 200 kV and fitted with an EDAX EDS system.

3. Results

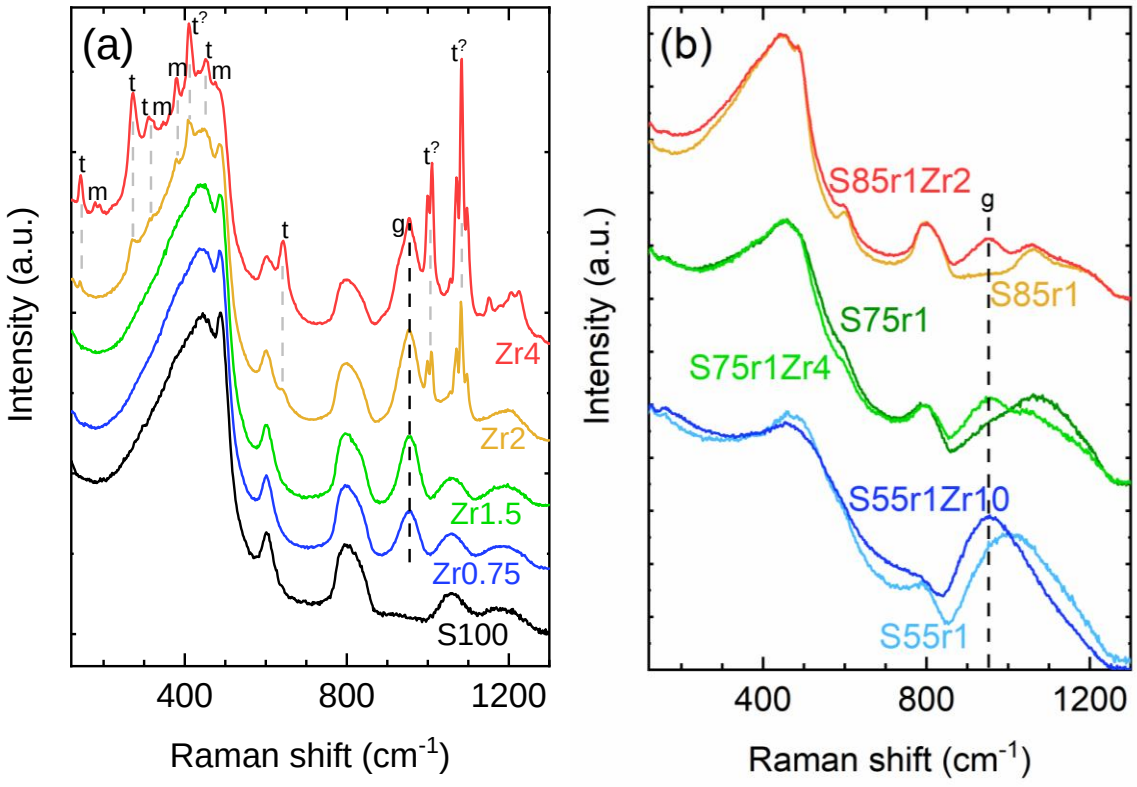

Figure 2. Raman spectra collected from: a) samples of base composition S100, doped with increasing amounts of ZrO_2 (0-4 mol%); b) glasses of base composition S85r1, S75r1 and S55r1 with and without ZrO_2, in the maximum investigated addition still yielding an

amorphous material. In both cases, *g* marks the position of the most intense Raman feature associated with the incorporation of Zr^{4+} in the amorphous (alumino)silicate network; other labels: *t* for t-ZrO_2 [30], $t^?$ for bands clearly associated with t-ZrO_2 but absent in the literature (see discussion in the text), *m* for m-ZrO_2 [30].

Raman measurements were used to verify the successful incorporation of ZrO_2 in the amorphous structure of the synthesized (alumino)silicate glasses. As expected, the spectrum of undoped S100 (Fig. 2-a) exhibited the typical vibrational features of pure SiO_2, i.e. broad asymmetric bands at 450 and 800 cm^{-1} associated with the vibrations of Si-O-Si linkages, sharper "defect" lines at 490 and 600 cm^{-1} stemming from the breathing modes of four- and three-membered tetrahedral rings and, above 1000 cm^{-1}, the envelope for the stretching of bridging oxygens about SiO_4 tetrahedra [31–35]. In turn, an additional relatively broad band was observed in the spectra of ZrO_2-doped S100 samples, centered at ~950 cm^{-1} and growing in intensity with increasing ZrO_2 content; a similar vibrational feature has been previously observed in SiO_2-ZrO_2 gels [36], ZrO_2-bearing borosilicate [37,38] and aluminosilicate glasses and assigned to the stretching of bridging oxygens about SiO_4 Q^3 units linked to a Zr polyhedron [39]. S100Zr2 and S100Zr4 could not be fully vitrified and accordingly display several supplementary sharp bands stemming from crystalline material (see treatment below).

Similar considerations can be applied to the Raman spectra of S85r1, S75r1 and S55r1 (Fig. 2-b): their undoped spectra manifested a consistent broadening at low wavenumbers and a gradual downshift at high wavenumbers with respect to S100, due to the progressive Al_2O_3 and MgO enrichment of the glass. These observations agree with previous Raman investigations in the MAS system [40]. Again, the addition of ZrO_2 brought about the appearance of a supplementary vibrational feature at ~950 cm^{-1}, which can be therefore univocally associated with the incorporation of this oxide in the amorphous (alumino)silicate

structure. The spectrum of the Al-richer samples (especially S55r1) appeared moreover to be more profoundly impacted by the ZrO_2 doping, with a further smearing out of the original silicate bands and a clear downshift of the high-wavenumber vibrational envelope. Note that the shown spectra correspond to the highest experimented ZrO_2 contents which yielded fully amorphous samples along the silica-cordierite join (see Figures S6, S7 and S8 of the SI section for the spectra of all synthesized samples).

The only crystalline phase contained in samples located slightly above the ZrO_2 saturation limit (Fig. 1-b) was invariably t-ZrO_2, as confirmed by the comparison of the observed Raman bands (at roughly 145, 270, 320, 450, 600 and 650 cm^{-1} in Figs. 2-a and 3) with previous references [30]. Despite the lack of literature correspondence, the sharp features observed at 410 cm^{-1} and above 1000 cm^{-1} (see Discussion) were clearly related to the same phase. This whole set of Raman bands appeared also after annealing above T_g samples that were initially obtained as glasses, as inferable from the spectra of S75r1Zr4ht and S55r1Zr8ht. At higher doping levels, the additional formation of m-ZrO_2 took place during quenching, such as in S55r1Zr20 and S100Zr4. These results were corroborated by parallel XRD measurements (Fig. 3-b).

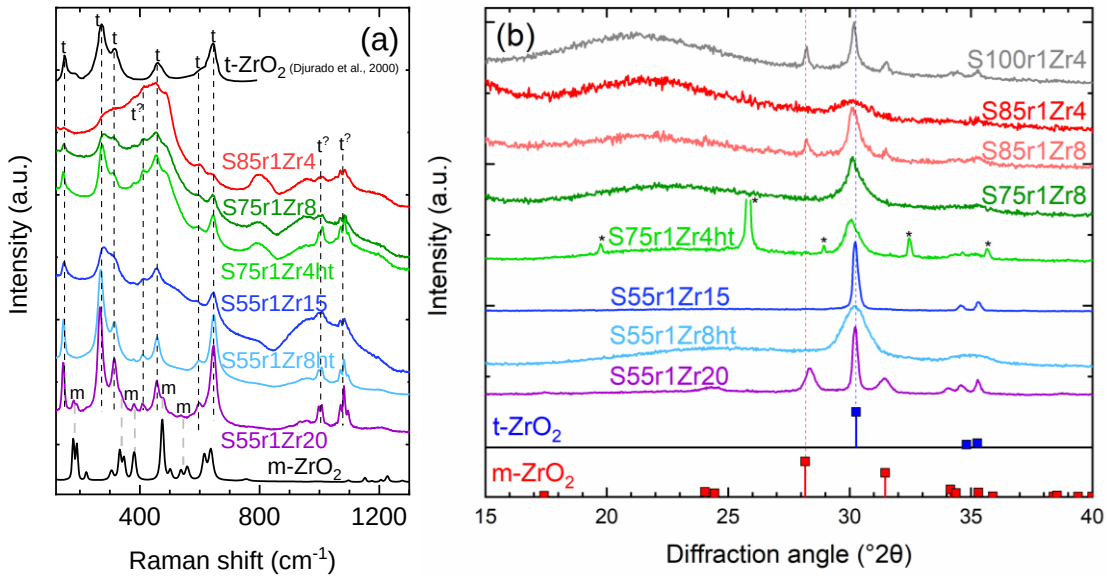

Figure 3. a) Raman spectra collected from samples of S85r1, S75r1 and S55r1 base composition, devitrified during cooling from the melt or after controlled secondary heat treatments (-*ht* suffix); the spectrum of the employed m-ZrO_2 raw material is provided for comparison. Labels: *t* for t-ZrO_2 [30], $t^?$ for bands clearly associated with t-ZrO_2 but absent in the literature (see discussion in the text), *m* for m-ZrO_2 [30]. b) XRD measurements performed on several as-quenched and heat-treated samples in comparison to the PDF cards of m-ZrO_2 [41] [ICDD 00-037-1484] and t-ZrO_2 [42] [ICDD 00-050-1089].

Interestingly, the capability of peraluminous (and MgO-free) samples to incorporate ZrO_2 in a fully amorphous structure was found to be significantly higher than that of their counterparts along the silica-cordierite join. While S85r1Zr4 contained t-ZrO_2, S85r0Zr4 was completely amorphous (Fig. 4); at lower SiO_2 content, S75r1Zr8 located above the glass saturation limit for ZrO_2, while S75r0.4Zr8 and S75r0Zr8 showed no visible sign of devitrification. The Al_2O_3 excess particularly emerged as crucial when examining the S55 series: S55r1Zr15 and S55r0.5Zr15 devitrified during cooling, whereas the Al_2O_3-richer samples S55r0.2Zr15 and S55r0Zr15 were totally amorphous. The Raman spectra underwent again a gradual broadening of their features (including the characteristic band at ~950 cm^{-1}) as the SiO_2 content of the glasses reduced.

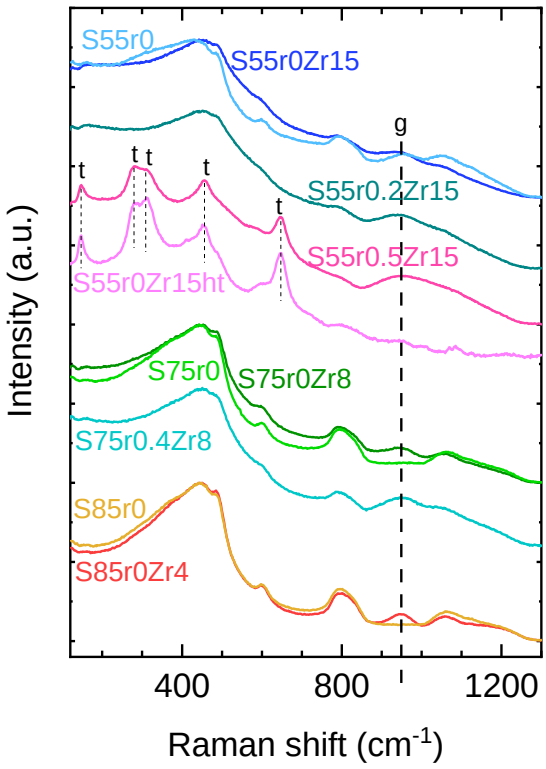

Figure 4. Raman spectra of various samples quenched on the peraluminous side of the MgO-Al_2O_3-SiO_2 ternary system, with and without ZrO_2 doping; *g* signals the position of the most intense Raman feature associated with the incorporation of Zr^{4+} in the amorphous (alumino)silicate network, *t* for t-ZrO_2 [30].

All amorphous samples with an excess of Al_2O_3 over MgO were analyzed by TEM to investigate their nanostructure, since base compositions S75r0 and especially S55r0 and S55r0.2 exhibited a noticeable opalescence with or without the addition of ZrO_2 (Fig. S3 of the SI section). Bright-field micrographs (Fig. 5) revealed the emergence of pervasive amorphous phase separation in all these peraluminous samples, embodied by the intergrowth of a high contrast (and therefore ZrO_2-rich) phase and a low-contrast one. Some of the materials (e.g. S85r0Zr4, S55r0.2Zr15, S55r0Zr15) exhibited a stronger analogy to

nanostructures typically assigned to a nucleation-growth mechanism, whereas the others matched more closely with the result of a spinodal decomposition or exhibited an intermediate character [43]. In sample S85r0 particularly, phase separation was only incipient and displayed diffused interfaces, making its recognition rather challenging. The average size of phase-separated domains (Fig. 5-g) was estimated in all samples by measuring the diameter of pseudo-spherical particles (or the smallest dimension of irregularly shaped ones, assuming them to originate from coalescence) located in the thinnest electron-transparent regions (to avoid artifacts due to object overlap). The resulting values enabled to explain the different optical behaviors of the samples, as only the biggest sizes induced a noticeable opalescence, in agreement with the available models [44]. The following relations could be additionally extracted: (i) in absence of ZrO_2, the phase separation increased in size with an increasing Al/Si ratio; (ii) at a given Al/Si ratio, the addition of ZrO_2 brought about a substantial increment in size and contrast of the demixed domains; (iii) substitution of Al_2O_3 by MgO (at given ZrO_2 and SiO_2 contents) led to the opposite effect. Thanks to the particularly big size of phase separation in sample S55r0Zr15, EDX enabled also a reliable estimation of the composition of its demixed regions: the low-contrast droplets yielded an average of 63(6) mol% SiO_2, 25(3) mol% Al_2O_3 and 12(1) mol% ZrO_2, while the result for the enclosing high-contrast matrix was 27(2) mol% SiO_2, 50(1) mol% Al_2O_3 and 23(2) mol% ZrO_2.

We additionally characterized by TEM sample S85r1Zr4, which devitrified during cooling and was macroscopically transparent (see Figs. S3 and S10 of the SI section). It contained a population of crystalline nuclei with an average size between 5 and 10 nm in an otherwise homogeneous glass matrix. Selected area electron diffraction (SAED) patterns exhhibited continuous diffuse rings and provided *d*-spacings assignable to the structure of t-ZrO_2 (the two examples highlighted on Fig. S10 yielded 1.8(1) Å and 3.0(1) Å, respectively

corresponding to the (011) and (112) planes of t-ZrO_2 [42]), in agreement with Raman and XRD results.

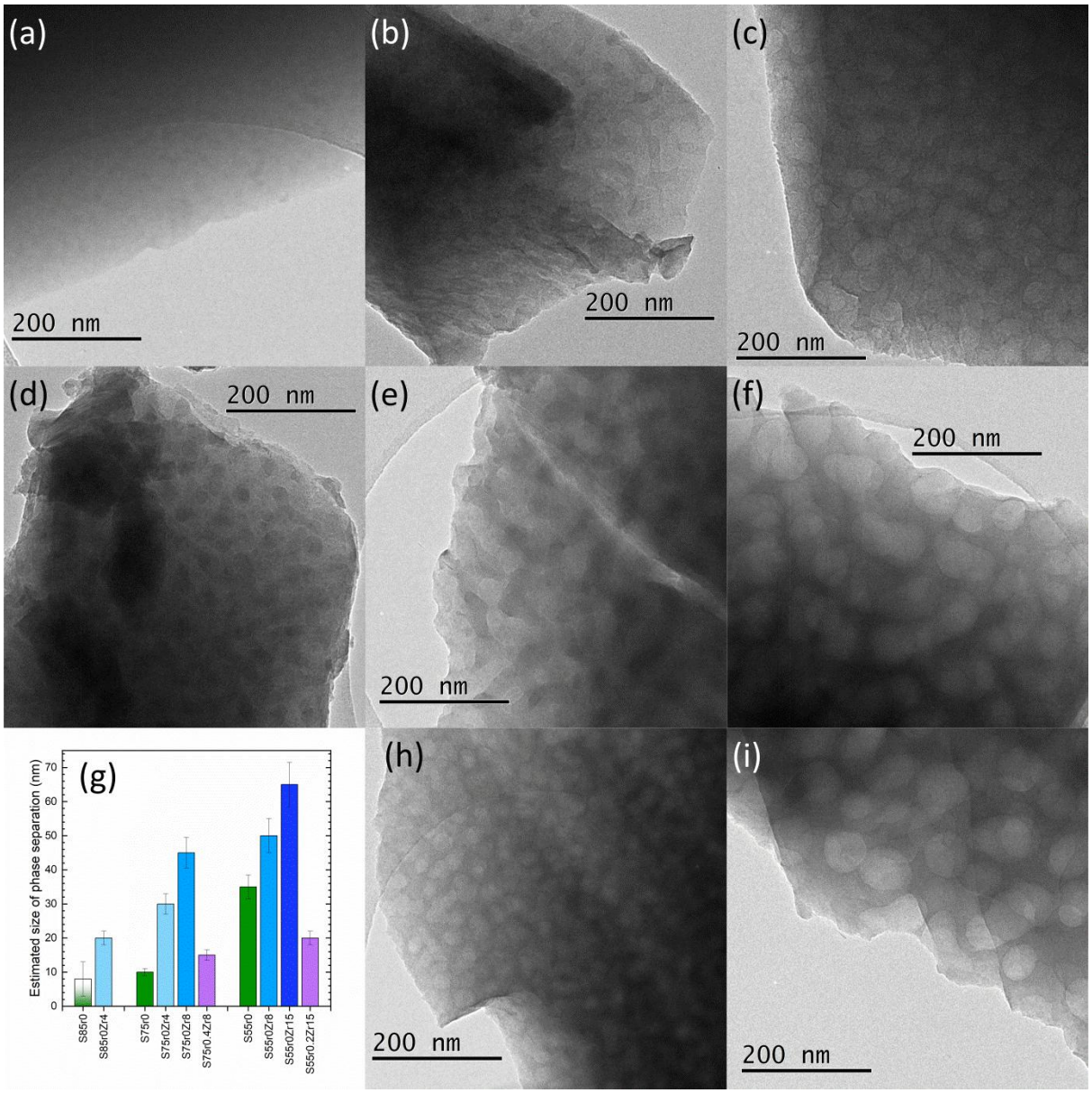

Figure 5. TEM bright-field micrographs of phase-separated samples: a) S85r0, b) S75r0, c) S55r0, d) S85r0Zr4, e) S75r0Zr8, f) S55r0Zr8, h) S55r0.2Zr15 and i) S55r0Zr15. g) Average size of the phase-separated regions in each sample, as estimated from TEM micrographs (see also Fig. S10 in the SI section).

4. Discussion

Containerless melting enabled us to screen a wide range of compositions and ZrO_2 doping levels in silicate melts, overcoming the temperature limitations of conventional melt-quenching and relating glass-forming ability purely to the tendency of ZrO_2 to nucleate homogeneously upon cooling. Our approach was mainly concerned with the identification of the ZrO_2 saturation limit in glasses quenched from above their liquidus temperatures; therefore, its results can be only limitedly compared with those of geoscientists investigating the subliquidus melt solubility of zircon as a function of temperature and composition [19–23]. However, our study confirms the key relevance of SiO_2 content and overall structural polymerization for the incorporation of Zr^{4+} in silicate glasses: the saturation threshold of this oxide increased steadily along the silica-cordierite join and was shown to be even higher at peraluminous compositions. Clearly, this must be due to the difficulty of a fully polymerized [SiO_4] tetrahedral network to accommodate high amounts of Zr^{4+}, which has been shown to assume preferentially a 6- or 7-fold oxygen coordination in SiO_2-ZrO_2 xerogels and in aluminosilicate glasses, sharing edges with adjacent (Si,Al)-polyhedra [6,9,39,45].

In a subaluminous soda lime glass, ZrO_2 oversaturation was previously correlated to a gradual shift from 6- to 8-fold oxygen coordination around Zr^{4+} ions, which would therefore prove less efficient than Al^{3+} ions (invariably 4-coordinated even at high ZrO_2 content) in the competition for charge-balancing modifier cations [39]. In MAS glasses, however, 5- and 6-fold-coordinated Al^{3+} species have been shown to be predominant even in the absence of ZrO_2, especially at peraluminous compositions [40]: the presence of these highly coordinated, modifier-like Al^{3+} species (and the resulting lower network rigidity) may therefore represent a key factor for the solubility of ZrO_2 in the glasses studied within this work. In fact, Raman spectra of our Al_2O_3-rich samples highlighted more extensive structural responses to the addition of ZrO_2 (the noted broadening and shift of Raman features); on the contrary, the spectrum of SiO_2 appeared barely affected by the dopant if not through the appearance of the

additional characteristic band at ~950 cm^{-1}, previously associated to occurrence of linkages between Q^3 units and Zr^{4+} oxygen polyhedra [39].

The inferred favorability of an Al_2O_3-rich environment for the amorphous incorporation of Zr^{4+} is reinforced by our TEM investigations. Phase separation could be observed already in samples belonging to the binary Al_2O_3-SiO_2 system, in which a metastable sub-liquidus immiscibility field is known from literature [46]. These materials were likely to demix during quenching, despite the relatively fast cooling rate of our ADL system (Fig. S2 of the SI section); the increment in size of the demixed regions with an increasing Al/Si ratio may therefore be associated to the expectably higher liquidus temperature and lower viscosity of Al_2O_3-richer melts, fostering nucleation and growth. As for Zr^{4+}, it was found to preferentially segregate in phase-separated regions with the highest Al/Si ratio, further increasing their size. This is indeed not surprising if one considers that a glass-forming region has been previously determined by plasma-spraying or melt-extraction at intermediate compositions of the binary Al_2O_3-ZrO_2 system [47–49]. On the contrary, an addition of MgO appeared to reduce the extent of phase separation, in analogy to the effect of alkali oxides such as Na_2O previously reported in similarly immiscible systems [50]. Other authors reported unavoidable nanoscale chemical heterogeneity (below the resolution of our TEM) even in a melt-quenched glass with virtually the same stoichiometry as our S75r1Zr4 sample [28], in which MgO equals Al_2O_3. The tendency towards heterogeneity and phase separation may therefore be inherent to the whole MgO-Al_2O_3-SiO_2 system, especially if ZrO_2 is added to compositions locating between the above-mentioned Al_2O_3-SiO_2 metastable immiscibility field [46] and, on the other side, a stable liquid immiscibility region in the MgO-SiO_2 binary system [51]. The heterogeneous distribution of ZrO_2 at the nanoscale was also related to the ability of these materials to nucleate t-ZrO_2 crystals during secondary annealing and yield technologically relevant glass-ceramics [9,28,52]. Overall, our results

complement the available literature and provide a solid fundamental starting point for the future compositional design of homogeneous glasses containing ZrO_2 or, in turn, for the exploitation of incipient heterogeneity and phase separation in the quest for novel transparent glass-ceramic materials, as recently demonstrated in immiscible zinc gallogermanate glasses [50].

Concerning now the ZrO_2 crystals in the devitrified samples, our observations are in line with the works of previous authors: t-ZrO_2 was already shown to precipitate preferentially from SiO_2-ZrO_2 plasma-sprayed melts [47] and the occurrence of this metastable polymorph was explained in terms of an energy minimization due to the high surface energy of the nanocrystals and/or associated to the mechanical constraints exerted by the surrounding glassy phase [30,47,53]. A chemical stabilization by Al_2O_3- and/or MgO-doping was instead previously speculated in the MAS system [54]: this might be at the origin of the substantial broadening of the t-ZrO_2 Raman bands in our MAS samples (Fig. 3), especially if compared with the spectra of S100Zr2 and S100Zr4 (Fig. 2). In turn, the additional bands observed in our spectra at 410 cm^{-1} and above 1000 cm^{-1}, though absent in the literature references for t-ZrO_2 [30], were clearly related to the formation of this phase, the only one detectable by XRD. They may be tentatively assigned to the presence of Si-O-Zr linkages in the nanocrystals, given the similarity of their positions with those of the main bands of zircon $ZrSiO_4$ (see for example [RRUFF ID: R050034] [55]), their peculiar sharpness in S100 samples and, conversely, their absence in Al_2O_3-rich samples such as S55r0Zr15ht and S55r0.5Zr15.

Crystals formed during melt devitrification or secondary glass annealing appeared virtually identical in our Raman spectra; similarly, the TEM micrographs of S85r1Zr4 (Fig. S10), devitrified during cooling, closely resembled the homogeneously distributed nanocrystals typically encountered in glass-ceramics. It is therefore possible to conclude that

ZrO_2 crystallization must have taken place at relatively deep undercooling during quenching, probably driven by the temperature-dependent oversaturation of the melt and by the gradual slow-down of the quenching rate in our ADL system (Fig. S2 in the SI section). Such a crystallization mechanism may indeed open up more direct pathways to obtain transparent nanocrystallized materials by controlled cooling from the melt, bypassing the vitrification stage which is presently inevitable in conventional glass-ceramic production [56]. On the contrary, the adoption of a different levitation gas with higher thermal conductivity (such as O_2) and the production of smaller glass beads could have probably enabled an even higher ZrO_2 incorporation than documented in this study, by increasing the quenching rate; nevertheless, the identified compositional trends would still be valid. Regarding the appearance of m-ZrO_2 at higher degrees of supersaturation, it is to be attributed to the bigger ZrO_2 crystallite size or, possibly, to the presence of unmelted residues.

5. Conclusion

Our study has shed new light on the chemical constraints influencing the saturation threshold of ZrO_2 in aluminosilicate melts, paving the way for a smarter compositional design of technical glasses and glass-ceramics based on this oxide, e.g. by controlled cooling from the melt, exploiting phase separation or by conventional glass-ceramic processing. SiO_2 content and overall polymerization degree were found to be the main factors influencing the successful incorporation of Zr^{4+} in an amorphous network, with a crucial role played by the structural versatility of Al^{3+}. Concurrently, the chemical heterogeneity of as-quenched materials emerged once more as a preeminent feature of MAS glasses doped with ZrO_2, evoking alternative compositional approaches for the development of novel functional materials.

Acknowledgements

Alessio Zandonà wishes to acknowledge the Deutsche Forschungsgemeinschaft (DFG) for funding his research through the Walter Benjamin Program, grant n. ZA 1188/1-1. The authors are grateful to the ICMN laboratory (Orléans, France) for TEM access and to the French Agency for Research (Agence Nationale de la Recherche, ANR) for its financial support through the Equipex Planex ANR-11-EQPX-36.

References

[1] E.R. Begley, P.O. Herndon, 8 - Zirconia-Alumina-Silica Refractories, in: A.M. Alper (Ed.), Refractory Materials, Elsevier, 1971: pp. 185–208. https://doi.org/10.1016/B978-0-12-053304-6.50016-3.

[2] K. Kamiya, S. Sakka, Y. Tatemichi, Preparation of glass fibres of the ZrO2-SiO2 and Na2O-ZrO2-SiO2 systems from metal alkoxides and their resistance to alkaline solution, Journal of Materials Science. 15 (1980) 1765–1771. https://doi.org/10.1007/BF00550596.

[3] R.G. Simhan, Chemical durability of ZrO2 containing glasses, Journal of Non-Crystalline Solids. 54 (1983) 335–343. https://doi.org/10.1016/0022-3093(83)90074-1.

[4] M. Lobanova, A. Ledieu, P. Barboux, F. Devreux, O. Spalla, J. Lambard, Effect of ZrO2 on the glass durability, MRS Online Proceedings Library. 713 (2002) 151. https://doi.org/10.1557/PROC-713-JJ15.1.

[5] S. Gin, P. Jollivet, M. Fournier, C. Berthon, Z. Wang, A. Mitroshkov, Z. Zhu, J.V. Ryan, The fate of silicon during glass corrosion under alkaline conditions: A mechanistic and kinetic study with the International Simple Glass, Geochimica et Cosmochimica Acta. 151 (2015) 68–85. https://doi.org/10.1016/j.gca.2014.12.009.

[6] O. Dargaud, L. Cormier, N. Menguy, L. Galoisy, G. Calas, S. Papin, G. Querel, L. Olivi, Structural role of Zr4+ as a nucleating agent in a MgO–Al2O3–SiO2 glass-ceramics: A combined XAS and HRTEM approach, Journal of Non-Crystalline Solids. 356 (2010) 2928–2934. https://doi.org/10.1016/j.jnoncrysol.2010.05.104.

[7] M. Dressler, B. Rüdinger, J. Deubener, Crystallization kinetics in a lithium alumosilicate glass using SnO2 and ZrO2 additives, Journal of Non-Crystalline Solids. 389 (2014) 60–65. https://doi.org/10.1016/j.jnoncrysol.2014.02.008.

[8] C. Patzig, M. Dittmer, A. Gawronski, T. Höche, C. Rüssel, Crystallization of ZrO2-nucleated MgO/Al2O3/SiO2 glasses – a TEM study, CrystEngComm. 16 (2014) 6578–6587. https://doi.org/10.1039/C4CE00636D.

[9] L. Cormier, O. Dargaud, G. Calas, C. Jousseaume, S. Papin, N. Trcera, A. Cognigni, Zr environment and nucleation role in aluminosilicate glasses, Materials Chemistry and Physics. 152 (2015) 41–47. https://doi.org/10.1016/j.matchemphys.2014.12.008.

[10] S. Seidel, M. Dittmer, W. Höland, C. Rüssel, High-strength, translucent glass-ceramics in the system MgO-ZnO-Al2O3-SiO2-ZrO2, Journal of the European Ceramic Society. 37 (2017) 2685–2694. https://doi.org/10.1016/j.jeurceramsoc.2017.02.039.

[11] E. Kleebusch, C. Patzig, M. Krause, Y. Hu, T. Höche, C. Rüssel, The formation of nanocrystalline ZrO2 nuclei in a Li2O-Al2O3-SiO2 glass – a combined XANES and TEM study, Scientific Reports. 7 (2017) 10869. https://doi.org/10.1038/s41598-017-11228-7.

[12] M. McCoy, W.E. Lee, A.H. Heuer, Crystallization of MgO-Al2O3-SiO2-ZrO2 Glasses, Journal of the American Ceramic Society. 69 (1986) 292–296. https://doi.org/10.1111/j.1151-2916.1986.tb07430.x.

[13] M. NOGAMI, M. TOMOZAWA, ZrO2-Transformation-Toughened Glass-Ceramics Prepared by the Sol-Gel Process from Metal Alkoxides, Journal of the American

Ceramic Society. 69 (1986) 99–102. https://doi.org/10.1111/j.1151-2916.1986.tb04709.x.

[14] F.H. Margha, S.A.-H.M. Abdel-Hameed, N.A.E.-S. Ghonim, S.A. Ali, S. Kato, S. Satokawa, T. Kojima, Crystallization behaviour and hardness of glass ceramics rich in nanocrystals of ZrO2, Ceramics International. 35 (2009) 1133–1137. https://doi.org/10.1016/j.ceramint.2008.05.009.

[15] Y. Nobuta, Y. Takahashi, T. Miyazaki, N. Terakado, N. Onoue, T. Shinozaki, T. Fujiwara, Formation and photoluminescence of zirconia dendrites in borosilicate glass-ceramics, Journal of the Ceramic Society of Japan. 125 (2017) 343–347. https://doi.org/10.2109/jcersj2.17001.

[16] Y. Liu, D. Yang, L. Riekehr, H. Engqvist, L. Fu, W. Xia, Combining good mechanical properties and high translucency in yttrium-doped ZrO2-SiO2 nanocrystalline glass-ceramics, Journal of the European Ceramic Society. (2021). https://doi.org/10.1016/j.jeurceramsoc.2021.09.047.

[17] C. Bettinali, G. Ferraresso, J.W. Manconi, Thermoluminescence of ZrO2, J. Chem. Phys. 50 (1969) 3957–3961. https://doi.org/10.1063/1.1671655.

[18] A.H. Heuer, Transformation Toughening in ZrO2-Containing Ceramics, Journal of the American Ceramic Society. 70 (1987) 689–698. https://doi.org/10.1111/j.1151-2916.1987.tb04865.x.

[19] A.J. Ellison, P.C. Hess, Solution behavior of +4 cations in high silica melts: petrologic and geochemical implications, Contributions to Mineralogy and Petrology. 94 (1986) 343–351. https://doi.org/10.1007/BF00371443.

[20] P. Boehnke, E.B. Watson, D. Trail, T.M. Harrison, A.K. Schmitt, Zircon saturation re-revisited, Chemical Geology. 351 (2013) 324–334. https://doi.org/10.1016/j.chemgeo.2013.05.028.

[21] F. Gervasoni, S. Klemme, E.R.V. Rocha-Júnior, J. Berndt, Zircon saturation in silicate melts: a new and improved model for aluminous and alkaline melts, Contributions to Mineralogy and Petrology. 171 (2016) 21. https://doi.org/10.1007/s00410-016-1227-y.

[22] A. Borisov, L. Aranovich, Zircon solubility in silicate melts: New experiments and probability of zircon crystallization in deeply evolved basic melts, Chemical Geology. 510 (2019) 103–112. https://doi.org/10.1016/j.chemgeo.2019.02.019.

[23] T. Shao, Y. Xia, X. Ding, Y. Cai, M. Song, Zircon saturation model in silicate melts: a review and update, Acta Geochimica. 39 (2020) 387–403. https://doi.org/10.1007/s11631-019-00384-4.

[24] D.A. Winborne, P.C. Nordine, D.E. Rosner, N.F. Marley, Aerodynamic levitation technique for containerless high temperature studies on liquid and solid samples, Metallurgical Transactions B. 7 (1976) 711–713. https://doi.org/10.1007/BF02698607.

[25] J.K.R. Weber, The Containerless Synthesis of Glass, International Journal of Applied Glass Science. 1 (2010) 248–256. https://doi.org/10.1111/j.2041-1294.2010.00026.x.

[26] K. Yoshimoto, A. Masuno, H. Inoue, Y. Watanabe, Transparent and High Refractive Index La2O3–WO3 Glass Prepared Using Containerless Processing, Journal of the American Ceramic Society. 95 (2012) 3501–3504. https://doi.org/10.1111/j.1551-2916.2012.05439.x.

[27] Z. Mao, J. Duan, X. Zheng, M. Zhang, L. Zhang, H. Zhao, J. Yu, Study on optical properties of La2O3–TiO2–Nb2O5 glasses prepared by containerless processing, Ceramics International. 41 (2015) S51–S56. https://doi.org/10.1016/j.ceramint.2015.03.154.

[28] O. Dargaud, L. Cormier, N. Menguy, G. Patriarche, G. Calas, Mesoscopic scale description of nucleation processes in glasses, Appl. Phys. Lett. 99 (2011) 021904. https://doi.org/10.1063/1.3610557.

[29] A. Zandona, B. Rüdinger, O. Hochrein, J. Deubener, Crystallization and SiAl ordering in cordierite glass-ceramics, Journal of Non-Crystalline Solids. 498 (2018) 160–166. https://doi.org/10.1016/j.jnoncrysol.2018.06.013.

[30] E. Djurado, P. Bouvier, G. Lucazeau, Crystallite Size Effect on the Tetragonal-Monoclinic Transition of Undoped Nanocrystalline Zirconia Studied by XRD and Raman Spectrometry, Journal of Solid State Chemistry. 149 (2000) 399–407. https://doi.org/10.1006/jssc.1999.8565.

[31] F.L. Galeener, J.C. Mikkelsen, Vibrational dynamics in O18 -substituted vitreous SiO2, Phys. Rev. B. 23 (1981) 5527–5530. https://doi.org/10.1103/PhysRevB.23.5527.

[32] F.L. Galeener, Planar rings in vitreous silica, Journal of Non-Crystalline Solids. 49 (1982) 53–62. https://doi.org/10.1016/0022-3093(82)90108-9.

[33] F.L. Galeener, A.E. Geissberger, Vibrational dynamics in 30Si-substituted vitreous SiO2, Physical Review B. 27 (1983) 6199–6204.

[34] R.A. Barrio, F.L. Galeener, E. Martínez, R.J. Elliott, Regular ring dynamics in AX 2 tetrahedral glasses, Phys. Rev. B. 48 (1993) 15672–15689. https://doi.org/10.1103/PhysRevB.48.15672.

[35] P.F. Mcmillan, B.T. Poe, P. Gillet, B. Reynard, A study of SiO2 glass and supercooled liquid to 1950 K via high-temperature Raman spectroscopy, Geochimica et Cosmochimica Acta. 58 (1994) 3653–3664.

[36] S.W. Lee, R.A. Condrate, The infrared and Raman spectra of ZrO2-SiO2 glasses prepared by a sol-gel process, Journal of Materials Science. 23 (1988) 2951–2959. https://doi.org/10.1007/BF00547474.

[37] D.A. McKeown, I.S. Muller, A.C. Buechele, I.L. Pegg, C.A. Kendziora, Structural characterization of high-zirconia borosilicate glasses using Raman spectroscopy, Journal

of Non-Crystalline Solids. 262 (2000) 126–134. https://doi.org/10.1016/S0022-3093(99)00691-2.

[38] F. Angeli, T. Charpentier, D. De Ligny, C. Cailleteau, Boron Speciation in Soda-Lime Borosilicate Glasses Containing Zirconium, Journal of the American Ceramic Society. 93 (2010) 2693–2704. https://doi.org/10.1111/j.1551-2916.2010.03771.x.

[39] M. Ficheux, E. Burov, G. Aquilanti, N. Trcera, V. Montouillout, L. Cormier, Structural evolution of high zirconia aluminosilicate glasses, Journal of Non-Crystalline Solids. 539 (2020) 120050. https://doi.org/10.1016/j.jnoncrysol.2020.120050.

[40] D.R. Neuville, L. Cormier, V. Montouillout, P. Florian, F. Millot, J.-C. Rifflet, D. Massiot, Amorphous materials: Properties, structure, and durability: Structure of Mg- and Mg/Ca aluminosilicate glasses: 27Al NMR and Raman spectroscopy investigations:, American Mineralogist. 93 (2008) 1721–1731. https://doi.org/doi:10.2138/am.2008.2867.

[41] H.F. McMurdie, M.C. Morris, E.H. Evans, B. Paretzkin, W. Wong-Ng, C.R. Hubbard, Standard X-Ray Diffraction Powder Patterns from The JCPDS Research Associateship, Powder Diffraction. 1 (1986) 265–275. https://doi.org/10.1017/S0885715600011829.

[42] J. Málek, L. Beneš, T. Mitsuhashi, Powder diffraction data and Rietveld refinement of metastable t-ZrO2 at low temperature, Powder Diffraction. 12 (1997) 96–98. https://doi.org/10.1017/S0885715600009519.

[43] P.F. James, Liquid-phase separation in glass-forming systems, Journal of Materials Science. 10 (1975) 1802–1825. https://doi.org/10.1007/BF00554944.

[44] S. Hendy, Light scattering in transparent glass ceramics, Appl. Phys. Lett. 81 (2002) 1171–1173. https://doi.org/10.1063/1.1499989.

[45] G. Mountjoy, M.A. Holland, P. Gunawidjaja, G.W. Wallidge, D.M. Pickup, R.J. Newport, M.E. Smith, Comparing the Atomic Structures of Binary MO2-SiO2 (M = Ti,

Zr or Hf) Xerogels, Journal of Sol-Gel Science and Technology. 26 (2003) 161–164. https://doi.org/10.1023/A:1020774310142.

[46] S.H. Risbud, J.A. Pask, Mullite Crystallization from SiO2-Al2O3 Melts, Journal of the American Ceramic Society. 61 (1978) 63–67. https://doi.org/10.1111/j.1151-2916.1978.tb09232.x.

[47] A. Krauth, H. Meyer, Über Abschreckmodifikationen und ihr Kristallwachstum in Systemen mit Zirkonoxid, Ber. Deut. Ker. Ges. 42 (1965) 61–102.

[48] J. McKittrick, G. Kalonji, T. Ando, Crystallization of a rapidly solidified Al2O3-ZrO2 eutectic glass, Journal of Non-Crystalline Solids. 94 (1987) 163–174. https://doi.org/10.1016/S0022-3093(87)80284-3.

[49] H.-J. Kim, Y.J. Kim, Amorphous phase formation of the pseudo-binary Al2O3–ZrO2 alloy during plasma spray processing, Journal of Materials Science. 34 (1999) 29–33. https://doi.org/10.1023/A:1004492919174.

[50] S. Chenu, E. Véron, C. Genevois, G. Matzen, T. Cardinal, A. Etienne, D. Massiot, M. Allix, Tuneable nanostructuring of highly transparent zinc gallogermanate glasses and glass-ceramics, Advanced Optical Materials. 2 (2014) 364–372.

[51] J.W. Greig, Immiscibility in silicate melts; Part I, American Journal of Science. s5-13 (1927) 1–44. https://doi.org/10.2475/ajs.s5-13.73.1.

[52] O. Dargaud, L. Cormier, N. Menguy, G. Patriarche, Multi-scale structuration of glasses: Observations of phase separation and nanoscale heterogeneities in glasses by Z-contrast scanning electron transmission microscopy, Journal of Non-Crystalline Solids. 358 (2012) 1257–1262. https://doi.org/10.1016/j.jnoncrysol.2012.02.026.

[53] R.C. Garvie, The Occurrence of Metastable Tetragonal Zirconia as a Crystallite Size Effect, J. Phys. Chem. 69 (1965) 1238–1243. https://doi.org/10.1021/j100888a024.

[54] O. Dargaud, G. Calas, L. Cormier, L. Galoisy, C. Jousseaume, G. Querel, M. Newville, In Situ study of Nucleation of Zirconia in an MgO–Al2O3–SiO2 Glass, Journal of the American Ceramic Society. 93 (2010) 342–344. https://doi.org/10.1111/j.1551-2916.2009.03409.x.

[55] B. Lafuente, R.T. Downs, H. Yang, N. Stone, 1. The power of databases: The RRUFF project, in: Highlights in Mineralogical Crystallography, De Gruyter, Berlin, Boston, 2015: pp. 1–30. https://doi.org/10.1515/9783110417104-003.

[56] J. Deubener, M. Allix, M.J. Davis, A. Duran, T. Höche, T. Honma, T. Komatsu, S. Krüger, I. Mitra, R. Müller, S. Nakane, M.J. Pascual, J.W.P. Schmelzer, E.D. Zanotto, S. Zhou, Updated definition of glass-ceramics, Journal of Non-Crystalline Solids. 501 (2018) 3–10. https://doi.org/10.1016/j.jnoncrysol.2018.01.033.

Figure Captions

Figure 1. a) Upper section of the MgO-Al_2O_3-SiO_2 ternary diagram, reporting the base glass compositions analyzed within this work. b) Summary of all samples synthesized within this work (see also Table 1): partially devitrified materials (as concomitantly determined by XRD and Raman) are identified by orange spheres, while fully amorphous samples are shown in blue (mind that all amorphous samples off the line $MgO = Al_2O_3$ were investigated by TEM and found to exhibit phase separation; see Fig. 5 and related discussion).

Figure 2. Raman spectra collected from: a) samples of base composition S100, doped with increasing amounts of ZrO_2 (0-4 mol%); b) glasses of base composition S85r1, S75r1 and S55r1 with and without ZrO_2, in the maximum investigated addition still yielding an amorphous material. In both cases, *g* marks the position of the most intense Raman feature associated with the incorporation of Zr^{4+} in the amorphous (alumino)silicate network; other labels: *t* for t-ZrO_2 [30], $t^?$ for bands clearly associated with t-ZrO_2 but absent in the literature (see discussion in the text), *m* for m-ZrO_2 [30].

Figure 3. a) Raman spectra collected from samples of S85r1, S75r1 and S55r1 base composition, devitrified during cooling from the melt or after controlled secondary heat treatments (-*ht* suffix); the spectrum of the employed m-ZrO_2 raw material is provided for comparison. Labels: *t* for t-ZrO_2 [30], $t^?$ for bands clearly associated with t-ZrO_2 but absent in the literature (see discussion in the text), *m* for m-ZrO_2 [30]. b) XRD measurements performed on several as-quenched and heat-treated samples in comparison to the PDF cards of m-ZrO_2 [41] [ICDD 00-037-1484] and t-ZrO_2 [42] [ICDD 00-050-1089].

Figure 4. Raman spectra of various samples quenched on the peraluminous side of the MgO-Al_2O_3-SiO_2 ternary system, with and without ZrO_2 doping; *g* signals the position of the most intense Raman feature associated with the incorporation of Zr^{4+} in the amorphous (alumino)silicate network, *t* for t-ZrO_2 [30].

Figure 5. TEM bright-field micrographs of phase-separated samples: a) S85r0, b) S75r0, c) S55r0, d) S85r0Zr4, e) S75r0Zr8, f) S55r0Zr8, h) S55r0.2Zr15 and i) S55r0Zr15. g) Average size of the phase-separated regions in each sample, as estimated from TEM micrographs (see also Fig. S10 in the SI section).